NJC

PAPER

View Article Online
View Journal | View Issue



Cite this: *New J. Chem.*, 2023, **47**, 19289

# Heterometallic Ru–Ir carbonyl clusters as catalyst precursors for hydrogenation and hydrogen transfer reactions†

Francesca Forti,[ab] Cristiana Cesari, *[ab] Marco Bortoluzzi,[c] Cristina Femoni,[a] Maria Carmela Iapalucci[a] and Stefano Zacchini[ab]

Received 25th July 2023,
Accepted 22nd September 2023

DOI: 10.1039/d3nj03478j

rsc.li/njc

Reaction of $[HRu_3(CO)_{11}]^-$ (**1**) with $[Ir(COD)Cl]_2$ in $CH_2Cl_2$ under a $H_2$ atmosphere afforded dihydride $[H_2Ru_3Ir(CO)_{12}]^-$ (**2**), which was quantitatively protonated to $H_3Ru_3Ir(CO)_{12}$ (**3**) by strong acids such as $HBF_4{\cdot}Et_2O$. The related mono-hydride $[HRu_3Ir(CO)_{12}]^{2-}$ (**4**) was obtained by deprotonation of **2** with a strong base such as KO$^t$Bu, or by the reaction of **1** with $[Ir(CO)_4]^-$ in refluxing THF. Hydride carbonyl clusters **2–4** were fully characterized by IR and $^1$H NMR spectroscopies, and the molecular structures of **2** and **3** were determined by single-crystal X-ray diffraction (SC-XRD). The location of the hydride ligands within the tetrahedral cages of these clusters was further corroborated by computational studies employing DFT methods. Clusters **2–4** were tested as catalyst precursors for transfer hydrogenation on the model substrate 4-fluoroacetophenone, using $^i$PrOH as a solvent and a hydrogen source. The results obtained using these heterometallic Ru–Ir clusters were compared to those using homometallic **1**, evidencing a significant difference, particularly regarding the effect of the base on catalysis. Heterometallic cluster **2** was also tested in the hydrogenation of *trans*-cinnamaldehyde in $^i$PrOH at refluxing temperature both under $N_2$ and $H_2$ atmospheres, and $H_2$ pressure.



## Introduction

Heterometallic complexes, clusters and nanoparticles find several applications in homogeneous and heterogeneous catalysis, due to synergistic effects of metal centres possessing different nature.[1–11] In this respect, molecular clusters and nanoclusters represent a link between metal complexes and metal nanoparticles.[12–21] Molecular clusters may be used in homogenous catalysis or as precursors of supported heterogeneous nanostructured catalysts.[22–25]

$[Ru_3Ir(CO)_{13}]^-$ showed high catalytic activity for the carbonylation of methanol.[26,27] $HRu_3Ir(CO)_{13}$ acted as an effective catalyst in the hydrogenation of diphenylacetylene to stilbene.[28] Several Ru–Ir complexes were employed in homogeneous catalysis for the hydrogenation of alkenes, alkynes, aldehydes and ketones.[25] Supported heterometallic Ru–Ir catalysts have been shown to produce $C_2$ oxygenates from syngas[29,30] and also to exhibit unusually high catalytic activity for the oxygen evolution reaction in the electrolysis of water.[31–34] Ru–Ir nanoparticles were employed for the catalytic hydrogenation of carbonyl compounds at room temperature and $H_2$ pressure.[35] Carbon-supported heterometallic Ru–Ir catalysts were used for selective and stable hydrodebromination of dibromomethane.[36] Hydrogenation of $CO_2$ was accomplished over mixed Ru–Ir catalysts.[37] Overall, it seems that Ru–Ir complexes and clusters might have very interesting catalytic properties, in view of synergistic effects between these two metals that are employed in catalysis often also as homometallic species.

Within this framework, we report an improved synthesis of the cluster $[H_2Ru_3Ir(CO)_{12}]^-$,[26,27,38] as well as the study of its protonation and deprotonation reactions, which resulted in a $[H_{3-n}Ru_3Ir(CO)_{12}]^{n-}$ ($n$ = 0–2) series of clusters. All the species were characterized by IR and $^1$H NMR spectroscopies, and their structures were determined by single-crystal X-ray diffraction (SC-XRD). The location of hydride ligands was complemented by computational studies. These heterometallic Ru–Ir clusters were tested as catalyst precursors for transfer hydrogenation of 4-fluoroacetophenone using $^i$PrOH as a solvent and a

[a] *Dipartimento di Chimica Industriale "Toso Montanari", Università di Bologna, Viale Risorgimento 4 – 40136, Bologna, Italy. E-mail: cristiana.cesari2@unibo.it*
[b] *Center for Chemical Catalysis – C3, Viale Risorgimento 4 – 40136, University of Bologna, Bologna, Italy*
[c] *Dipartimento di Scienze Molecolari e Nanosistemi, Ca' Foscari University of Venice, Via Torino 155 – 30175, Mestre (Ve), Italy*

† Electronic supplementary information (ESI) available: Supplementary experimental and computational figures and tables. Crystal data and collection details (PDF). DFT-optimized coordinates in the XYZ format (xyz). CCDC 2256428 ($[NEt_4][\mathbf{2}]$), 2256429 (**3**), 2256431 ($[NEt_4]_2[\mathbf{5}]$), and 2256432 ($[NEt_4]_2[\mathbf{6}]$), contain the supplementary crystallographic data for this paper. For ESI and crystallographic data in CIF or other electronic format see DOI: **https://doi.org/10.1039/d3nj03478j**

hydrogen source. $[H_2Ru_3Ir(CO)_{12}]^-$ was also employed as the catalyst precursor in hydrogenation of *trans*-cinnamaldehyde under both hydrogen transfer and direct $H_2$ hydrogenation conditions.

## Results and discussion

### Synthesis, characterization and molecular structures of $[H_{3-n}Ru_3Ir(CO)_{12}]^{n-}$ ($n$ = 0–2)

The di-hydride $[NEt_4][H_2Ru_3Ir(CO)_{12}]$ ([NEt$_4$][**2**]) is formed upon the reaction of $[NEt_4][HRu_3(CO)_{11}]$ ([NEt$_4$][**1**]) with 0.5 moles of $[Ir(COD)Cl]_2$ ($Ru_3$: Ir = 1 : 1) in $CH_2Cl_2$ under a $H_2$ atmosphere (Scheme 1), which favours the elimination of COD from Ir. On performing the same reaction under a $N_2$ atmosphere, **2** is obtained in a mixture with yet unidentified compounds. We suppose that the hydrogen atmosphere, unlike the $N_2$ inert gas atmosphere, enables the addition of the missing hydrogen atom to **1** and at the same time can function as a reducing agent for $[Ir(COD)Cl]_2$, so that selectivity is much higher. Reaction of **1** with $[Ir(COD)Cl]_2$ under a CO atmosphere leads to a completely different product, yet unidentified. We can also assume that the missing CO ligand in the structure of **2** is provided from a small amount of decomposed reagent **1**.

Compound **2** was identified by ESI-MS, IR spectroscopy and $^1$H NMR spectroscopy, and its structure was determined by SC-XRD as the [NEt$_4$] [**2**] salt.

The molecular structure of **2** found in [NEt$_4$][**2**] is comparable to that previously determined as the $[PPN]^+$ salt.[26,27,38] A similar structure was also adopted for the related Ru–Rh cluster $[H_2Ru_3Rh(CO)_{12}]^-$.[39] It consists of a $Ru_3Ir$ tetrahedron, where the edges of one $Ru_2Ir$ triangle are bridged by three μ-CO ligands (Fig. 1 and Table 1). The two μ-H hydride ligands are bridging the two Ru–Ru edges of the unique $Ru_3$ triangle not bearing μ-CO. This location of the hydride ligands is in agreement with the elongation of the μ-H bridged Ru–Ru edges (Table 1). One Ru atom is bonded to two μ-H and three terminal CO ligands. Ir and the two remaining Ru atoms are bonded to two terminal CO ligands, in addition to two μ-CO ligands, as well as one hydride in the case of the two Ru atoms. The presence of both terminal and edge bridging carbonyls is supported by IR analysis ($\nu_{CO}$ 2078(w), 2041(m), 2005(vs), 1973(m) cm$^{-1}$, and 1797(m) cm$^{-1}$ in the $CH_2Cl_2$ solution; Fig. S1 in the ESI†). The cluster displays *pseudo*-$C_{2v}$ symmetry and the two hydride ligands are equivalent, as also demonstrated

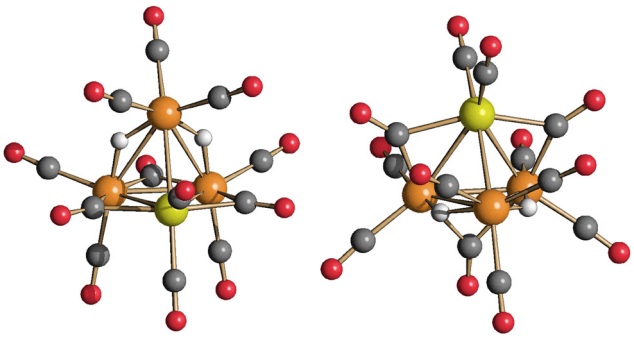

Fig. 1 Two views of the molecular structure of $[H_2Ru_3Ir(CO)_{12}]^-$ (**2**) (orange: Ru; yellow: Ir; red O; grey: C; white: H). All Ru–H distances were restrained to be same.

Table 1 Main bond lengths (Å) of $[H_2Ru_3Ir(CO)_{12}]^-$ (**2**) and $H_3Ru_3Ir(CO)_{12}$ (**3**) (see Scheme 2 for labelling). $CO_t$ refers to terminal carbonyls and $CO_b$ refers to edge bridging carbonyls

| | $[H_2Ru_3Ir(CO)_{12}]^-$ (**2**) | $H_3Ru_3Ir(CO)_{12}$ (**3**) |
|---|---|---|
| Ir(1)–Ru(1) | 2.7508(16) | 2.7401(6) |
| Ir(1)–Ru(2) | 2.7255(12) | 2.7414(6) |
| Ir(1)–Ru(3) | 2.7254(12) | 2.7454(6) |
| Ru(1)–Ru(2) | 2.9206(17) | 2.9193(8) |
| Ru(1)–Ru(3) | 2.9206(17) | 2.9093(8) |
| Ru(2)–Ru(3) | 2.760(2) | 2.9210(8) |
| Ir(1)–$CO_t$ | 1.84(2)–1.931(19) | 1.908(7)–1.918(7) |
| Ir(1)–$CO_b$ | 2.151(16) | — |
| Ru(1)–$CO_t$ | 1.895(17)–1.99(2) | 1.899(7)–1.940(8) |
| Ru(2)–$CO_t$ | 1.870(18)–1.914(16) | 1.910(8)–1.931(7) |
| Ru(2)–$CO_b$ | 2.042(17)–2.1127(16) | — |
| Ru(3)–$CO_t$ | 1.870(18)–1.914(16) | 1.895(7)–1.944(8) |
| Ru(3)–$CO_b$ | 2.042(17)–2.1127(16) | — |
| Ru(1)–H(1) | 1.60(6) | 1.80(3) |
| Ru(1)–H(2) | 1.60(6) | 1.80(3) |
| Ru(2)–H(2) | 1.60(6) | 1.79(3) |
| Ru(2)–H(3) | — | 1.79(3) |
| Ru(3)–H(1) | 1.60(6) | 1.79(3) |
| Ru(3)–H(3) | — | 1.79(3) |

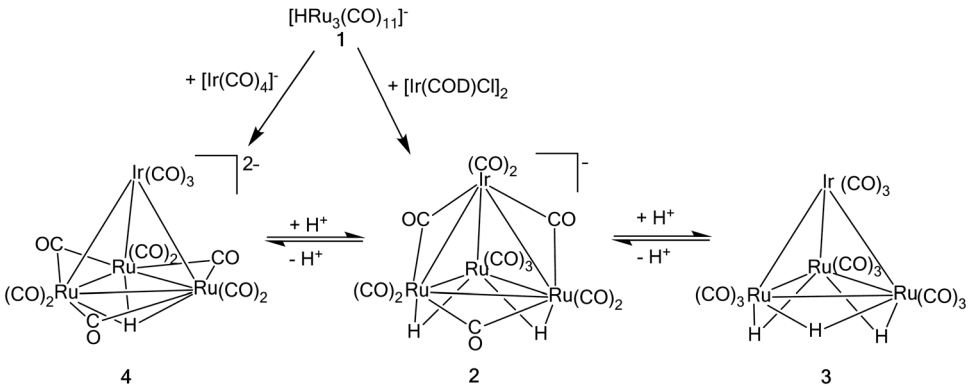


Scheme 1 Synthesis of **2**–**4**. $H^+$ is added using strong acids, such as $HBF_4{\cdot}Et_2O$; $H^+$ is removed using strong bases, such as KO$^t$Bu.

 

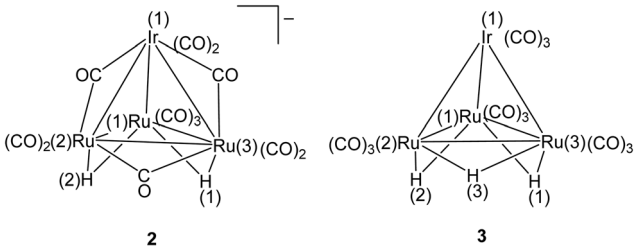


2 3

Scheme 2 Labelling of $[H_2Ru_3Ir(CO)_{12}]^-$ (**2**) and $H_3Ru_3Ir(CO)_{12}$ (**3**).

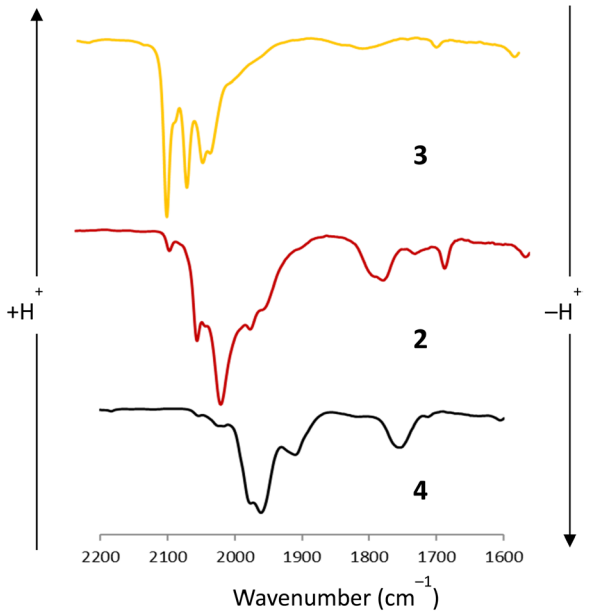


Fig. 2 IR spectra in the $\nu_{CO}$ region of $[H_{3-n}Ru_3Ir(CO)_{12}]^{n-}$ ($n$ = 0–2) in $CH_2Cl_2$. $H^+$ is added as $HBF_4{\cdot}Et_2O$ or $HCl{\cdot}Et_2O$, and removed with $KO^tBu$. See Scheme 3 for the stoichiometry.

by the presence of a singlet in the hydride region of the $^1H$ NMR spectrum ($\delta_H$ −20.7 ppm in $CD_2Cl_2$; Fig. S6 in the ESI†). The nature of $[H_2Ru_3Ir(CO)_{12}]^-$ in solution has been further corroborated by ESI-MS analysis, which shows a peak at $m/z$ 835 for the molecular mono-anion (Fig. S10 in the ESI†).

The position of the hydrides in **2** was further corroborated by DFT calculations. The {$Ru_3Ir$} tetrahedral structure with two hydrides bridging two Ru–Ru edges was also obtained starting from initial geometries with Ir–H interactions. The differences among the stationary points obtained from different initial structures are negligible. The computationally optimized ground state is in good agreement with the experimental data, and the RMSD is 0.178 Å. The greatest variation concerns the hydride positions, predicted to be slightly more far from the Ru centres with respect to the X-ray data (Fig. S11 in the ESI†). The unscaled simulated IR spectrum is shown in Fig. S16 in the ESI.† The vibrational frequencies are overestimated (about 7%) with respect to the experimental ones, as commonly occurs with IR simulations carried out at the DFT level with the harmonic approximation.

As previously reported for other hydride metal carbonyl clusters,[40–43] **2** undergoes reversible protonation/deprotonation reactions (Scheme 3). Thus, **2** is quantitatively converted into $H_3Ru_3Ir(CO)_{12}$ (**3**) upon the addition of a slight excess of a strong acid such as $HBF_4{\cdot}Et_2O$ or $HCl{\cdot}Et_2O$. By using $HCl{\cdot}Et_2O$, $[Ru_2Ir_2Cl_6(CO)_9]^{2-}$ (**5**) is obtained as a side product and, thus, a better yield of **3** is achieved with $HBF_4{\cdot}Et_2O$. The protonation may be reversed upon the addition of a strong base such as $KO^tBu$. Further addition of a 3 equivalent excess of $KO^tBu$ to **2** affords the mono-hydride di-anion $[HRu_3Ir(CO)_{12}]^{2-}$ (**4**). The process is reversed upon addition of a strong acid.

The mono-hydride di-anion **4** may be alternatively obtained from the reaction of **1** with $[Ir(CO)_4]^-$ in refluxing THF (Scheme 1). The structures of the new clusters **3** and **5** have been determined by SC-XRD as their **3** and $[NEt_4]_2$[**5**] crystals. Crystals of $[PPN]_2$[**4**] were of low quality and displayed high disorder, which hampered the full SC-XRD analysis of the structure of **4**. Preliminary data (crystal system, space group, and unit cell parameters) are included in the Experimental Section. These allowed the identification of the tetrahedral $Ru_3Ir$ metal cage of **4**, as well as the presence of twelve CO ligands and two $[PPN]^+$ cations. The structure of **4** was further investigated using computational methods (see below).

The protonation/deprotonation reactions of **2** were studied in solution by IR and $^1H$ NMR spectroscopies (Fig. 2, and Fig. S1–S8 in the ESI†).

The molecular structure of **3** is based on the same $Ru_3Ir$ tetrahedral metal core of **2** (Fig. 3 and Table 1). Nonetheless, the stereochemistry of the ligands is rather different. The trihydride **3**, in view of its neutral charge and reduced π-back donation, contains only terminal carbonyls, three per each metal atom. The three hydrides are edge-bridging on the three basal Ru–Ru edges. Cluster **3** possesses idealized $C_{3v}$ symmetry and, therefore, just a singlet is present in the hydride region of its $^1H$ NMR spectrum at $\delta_H$ −17.8 ppm (Fig. S8 in the ESI†). A similar structure was previously reported for $H_3Ru_3Rh(CO)_{12}$.[44] Even if the structure of **3** is unprecedented, a few phosphine derivatives of **3** have been previously reported.[38]

The DFT-optimized structure of **3** agrees well with the experimental outcomes, with a RMSD of 0.107 Å. The computed and experimental structures are superimposed in Fig. S12 in the ESI.† The simulated IR spectrum is reported in Fig. S16 in

$$[HRu_3Ir(CO)_{12}]^{2-} \underset{3\text{ eq. }KO^tBu}{\overset{1\text{ eq. }HBF_4}{\rightleftharpoons}} [H_2Ru_3Ir(CO)_{12}]^- \underset{3\text{ eq. }KO^tBu}{\overset{1.5\text{ eq. }HBF_4}{\rightleftharpoons}} [H_3Ru_3Ir(CO)_{12}]$$

**4** **2** **3**

Scheme 3 Protonation/deprotonation reactions of $[H_{3-n}Ru_3Ir(CO)_{12}]^{n-}$ ($n$ = 0–2).

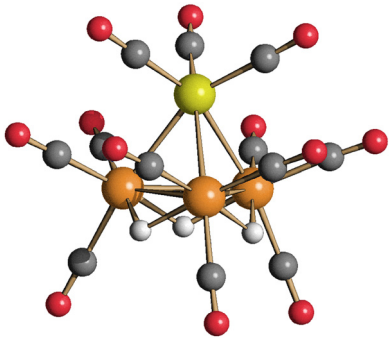

Fig. 3 Molecular structure of $H_3Ru_3Ir(CO)_{12}$ (**3**) (orange: Ru; yellow: Ir; red: O; grey: C; white: H). All Ru–H distances were restrained to be the same.

the ESI.† The investigation on other possible isomers of **3** afforded other two stationary points, where one of the hydrides is $\mu_3$-coordinated at the centre of a $\{Ru_2Ir\}$ face or it is bridging a Ru–Ir edge. As shown in Fig. S13 in the ESI,† both these isomers resulted however less stable than that experimentally observed.

The molecular structure of the mono-hydride di-anion **4** was only preliminarily determined by SC-XRD and, then, further optimized and investigated using DFT methods (Fig. 4). Based on this hybrid approach, the most likely structure of **4** consists of a $Ru_3Ir$ tetrahedron, as in the parent **2**. After some attempts, the computed structure depicted in Fig. 4 was selected as the most probable because it was the only one maintaining the same disposition of the carbonyl ligands deducted from the preliminary X-ray outcomes, *i.e.* three terminal carbonyls on the Ir centre, two terminal carbonyls for each Ru atom and three edge-bridging carbonyls located on the $Ru_3$ triangle. The superposition of the $\{Ru_3Ir(CO)_{12}\}$ fragments between the computed and preliminary X-ray structures is quite good, as observed in Fig. S14 in the ESI,† with a RMSD of 0.133 Å. The Cartesian coordinates of other possible isomers obtained from DFT calculations, with different dispositions of the CO ligands, are provided in the ESI† (Fig. S15). In the stationary point

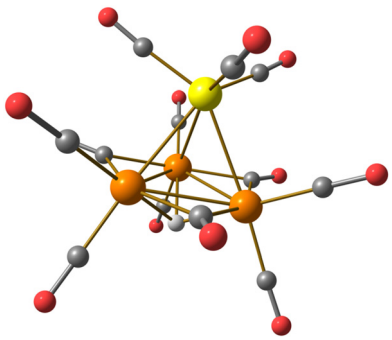

Fig. 4 PBEh-3c optimized structure of $[HRu_3Ir(CO)_{12}]^{2-}$ (**4**) (orange: Ru; yellow: Ir; red: O; grey: C). Selected computed average bond lengths (Å): Ru–Ru: 2.792; Ru–Ir: 2.818; Ru–$CO_t$: 1.841; Ru–$CO_b$: 2.109; Ru–H: 1.902. $CO_t$ refers to terminal carbonyls and $CO_b$ refers to edge bridging carbonyls.

considered (Fig. 4), the unique hydride caps the $Ru_3$ face with an average Ru–H distance of 1.902 Å, as in the case of $[HRu_4(CO)_{12}]^{3-}$[41] and $[HFe_4(CO)_{12}]^{3-}$.[45] The optimized geometry of **4** roughly belongs to the $C_{3v}$ point group ($R$ = 0.096). The presence of the hydride ligand has been supported by $^1$H NMR spectroscopy which shows a singlet at $\delta_H$ −19.9 ppm (Fig. S7 in the ESI†).

As in the case of **2**, **4** also contains nine terminal and three μ-CO ligands. Nonetheless, the three edge-bridging carbonyls are located on the $Ru_3$ triangle of **4**, and in a $Ru_2Ir$ triangle in the case of **2**. This further supports different numbers and locations of the hydride ligands in the two clusters.

It must be remarked that the related $[HFe_3M(CO)_{12}]^{2-}$ (M = Co, Rh, Ir) clusters adopt different structures. In the case of $[HFe_3Co(CO)_{12}]^{2-}$ and $[HFe_3Rh(CO)_{12}]^{2-}$,[46,47] three μ-CO ligands are located on a $Fe_2M$ triangle, with fourth μ-CO bridging the basal M and the apical Fe. The unique hydride is capping the $Fe_2M$ triangle. Conversely, $[HFe_3Ir(CO)_{12}]^{2-}$ displays only three μ-CO ligands on a $Fe_2Ir$ triangle, and the unique hydride bridges between the basal Ir and the apical $Fe(CO)_3$.[46]

The unscaled computed IR spectrum, reported in Fig. S16 in the ESI,† is in agreement with the experimental data. The simulated IR spectra of **2**, **3**, and **4** follow the trend observed in Fig. 2, with a shift towards higher frequencies of the CO stretching vibrations on reducing the negative charge of the clusters because of a lower degree of π-back-donation.

The Hirshfeld population analysis on **2**, **3** and **4** indicated that the partial charge on the hydrides is not directly related to the global charge of the clusters. The computed partial charge of the unique hydride in the doubly negatively charged cluster **4** is −0.102 a.u., while slightly more negative values were obtained for dihydride **2** (average value −0.118 a.u.) and neutral trihydride **3** (−0.117 a.u.).

It is worth noting that the structure shown in Fig. 4 is not the most stable isomer computationally found for **4**. Another stationary point with a completely different disposition of the carbonyl ligands and much lower symmetry resulted more stable by about 2.9 kcal mol$^{-1}$ (Gibbs free energy). As observed in Fig. S15 in the ESI,† in the energetically lowest isomer, the Ir centre is bonded to two terminal and two bridging carbonyl ligands. Another carbonyl bridges two Ru centres, each one bearing two terminal CO ligands. The last Ru centre interacts with three terminal CO. The hydride bridges $\{Ru(CO)_3\}$ and $\{Ru(CO)_2\}$ fragments. The energy gap with respect to the experimentally observed structure (based on the preliminary SC-XRD data) is however quite small, while the superimposition with the preliminary X-ray data is very poor. It is possible that the relative stability could be affected by anion–cation contacts and intramolecular interactions not accounted using *in vacuo* calculations. Another stationary point for **4**, where Ir is bonded only to one terminal carbonyl ligand and the hydride is $\mu_3$-briding two Ru and the Ir centres, is less stable than the other isomers (Fig. S15 in the ESI†).

In view of the fact that **2** and **3** are isostructural with $[H_2Ru_3Rh(CO)_{12}]^-$ and $H_3Ru_3Rh(CO)_{12}$, respectively, it was of interest to compare the structure of **4** with the related

 

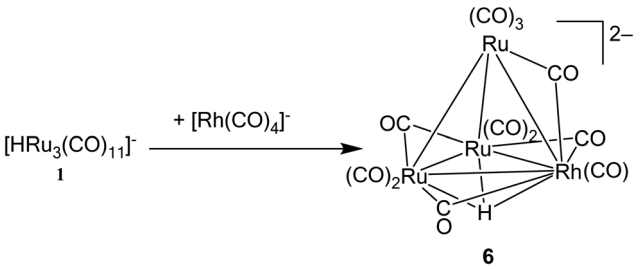


Scheme 4 Synthesis of **6**.

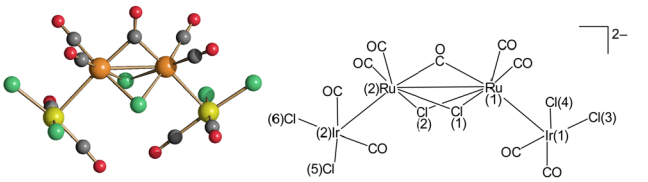


Fig. 6 Molecular structure of $[Ru_2Ir_2Cl_6(CO)_9]^{2-}$ (**5**) with a labelling scheme (orange: Ru; yellow: Ir; green: Cl; red: O; grey: C). Main bond distances (Å): Ru(1)–Ru(2) 2.9245(6), Ru(1)–Ir(1) 2.9061(4), Ru(2)–Ir(2) 2.9312(5), Ru(1)–Cl(1) 2.4727(12), Ru(1)–Cl(2) 2.4754(12), Ru(2)–Cl(1) 2.4759(12), Ru(2)–Cl(2) 2.4652(12), Ir(1)–Cl(3) 2.3315(14), Ir(1)–Cl(4) 2.3475(14), Ir(2)–Cl(5) 2.3473(13), Ir(2)–Cl(6) 2.3618(12).

$[HRu_3Rh(CO)_{12}]^{2-}$. Since its structure was not previously reported in the literature, $[HRu_3Rh(CO)_{12}]^{2-}$ (**6**) was prepared from **1** and $[Rh(CO)_4]^-$ (Scheme 4) and its molecular structure was determined by SC-XRD as the $[NEt_4]_2$ [**6**] salt (Fig. 5). The structure of **6** is different from that of **4** and similar to those of $[HFe_3Co(CO)_{12}]^{2-}$ and $[HFe_3Rh(CO)_{12}]^{2-}$.[46,47] Thus, the unique hydride is $\mu_3$-coordinated to a $Ru_2Rh$ triangle, whose three edges are bridged by three μ-CO ligands. A fourth μ-CO is bridging the basal Rh and apical Ru. The two Ru–Ru edges not bridged by μ-CO ligands are somehow hindered by terminal carbonyls, and this makes very unlikely that the unique hydride could be edge bridging rather than face capping. The location of the hydride on the $Ru_2Rh$ face is also in agreement with the fact that a doublet at $\delta_H$ −15.7 ppm with $^1J_{H\text{-}Rh}$ = 17 Hz is present in the $^1$H NMR spectrum of **6**. A similar $^1J_{H\text{-}Rh}$ coupling constant was observed in $[HFe_3Rh(CO)_{12}]^{2-}$, where the hydride is located on a $Fe_2Rh$ face.[47]

The DFT-optimized structure of **6** agrees with the X-ray structure, as observed in Fig. S17 in the ESI† (RMSD = 0.161 Å). The computed hydride position is a bit more far from the $\{Ru_2Rh\}$ plane with respect to the X-ray data. The simulated IR spectrum confirms the good overlap between the experimental and computed data (Fig. S17 in the ESI†). As previously occurred for the related Ir derivative **4**, the computational investigation afforded other stationary points for **6**, and, in particular, one is slightly more stable than the others (about 1.6 kcal mol$^{-1}$, Fig. S18 in the ESI†). The disposition of the carbonyl ligands is however different with respect to the experimental geometry (ruling out the possibility that this computed structure is present in the solid state), since two terminal CO are bonded to the Rh centre and only one CO bridges a Ru–Ru edge. In this case, the hydride bridges two Ru centres without a direct interaction with Rh. This disagrees with the $^1J_{H\text{-}Rh}$ coupling constant observed in solution, which is typical for $\mu_3$-H with direct coupling to Rh,[47] as experimentally observed. Finally, a structure geometrically analogous to that observed for **4** resulted less stable than the experimental one by about 4.6 kcal mol$^{-1}$.

It seems that the structures of $[HRu_3M(CO)_{12}]^{2-}$ and $[HFe_3M(CO)_{12}]^{2-}$ (M = Co, Rh, Ir) clusters result from a subtle balance between the sizes of the metals and their affinities for CO and hydride ligands.

The molecular structure of **5** is rather peculiar and may be viewed as composed of a $Ru_2(\mu\text{-}Cl)_2(\mu\text{-}CO)(CO)_4$ core where the two Ru atoms are directly bonded to two square–planar $[IrCl_2(CO)_2]^-$ complexes (Fig. 6).

The computed structure of **5** is in good agreement with the experimental one, with the RMSD being 0.361 Å. The superposition of the two structures is shown in Fig. S19 in the ESI.† The nature of the Ru–Ir interactions in **5** was investigated by means of AIM analysis. Comparable (3,−1) bond critical points were localized for both the Ru–Ir interactions, with an average electron density value of 0.245 e A$^{-3}$ and a potential energy density of −0.223 Hartree A$^{-3}$. The energy density is slightly

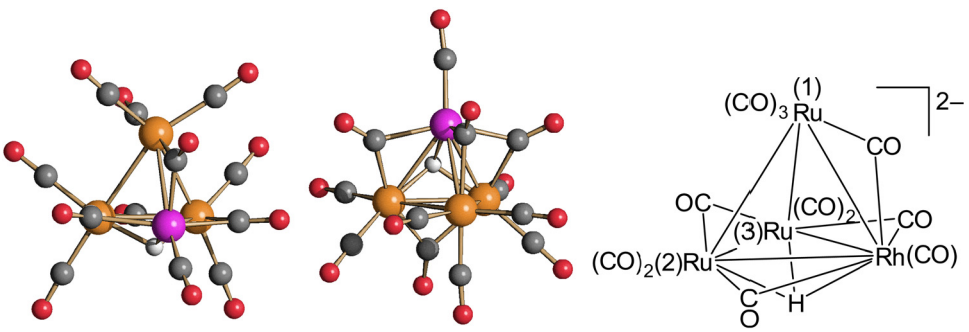


Fig. 5 Two views of the molecular structure of $[HRu_3Rh(CO)_{12}]^{2-}$ (**6**), with a labelling scheme (orange: Ru; purple: Rh; red: O; grey: C; white: H). Disordered Ru and Rh atoms were omitted. Main bond distances (Å) [data for the minor image are reported in square brackets; the hydride was not located in the minor image]: Rh–Ru(1) 2.816(2) [2.782(16)], Rh–Ru(2) 2.741(3) [2.757(17)], Rh–Ru(3) 2.780(3) [2.798(17)], Ru(1)–Ru(2) 2.852(3) [2.784(18)], Ru(1)–Ru(3) 2.883(3) [2.928(17)], Ru(2)–Ru(3) 2.787(3) [2.784(18)], Rh–H 1.90(2), Ru(2)–H 1.90(2), and Ru(3)–H 1.90(2). Restraints were applied to the Rh–H and Ru–H distances.

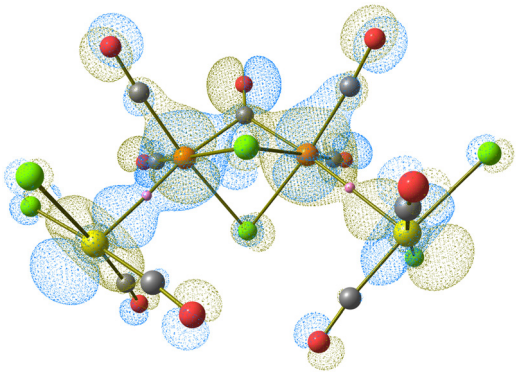

Fig. 7 DFT-optimized structure of **5** (orange: Ru; yellow: Ir; green: Cl; red: O; grey: C) with selected (3,−1) bond critical points indicated as small pink spheres and the occupied molecular orbital (surface isovalue = 0.02 a.u.) showing the best Ru–Ir bonding overlaps.

negative, −0.044 Hartree $A^{-3}$, while the Laplacian of electron density is positive, 3.852 e $A^{-5}$, according to Bianchi's definition of the metal–metal bond.[48] The two critical points are shown in Fig. 7, together with the occupied molecular orbital showing the best superposition between Ir and Ru. On the other hand, no (3,−1) bond critical point was localized between the Ru centres. The formal electron count for each Ru in a neutral $Ru_2(\mu\text{-}Cl)_2(\mu\text{-}CO)(CO)_4$ core without the Ru–Ru bond is 16 electrons; thus, two $[IrCl_2(CO)_2]^-$ fragments formally behave in **5** as ligands to saturate the coordination sphere of the Ru centres. The possible behaviour as the electron donor of $[IrCl_2(CO)_2]^-$ towards the Ru centre was supported by the charge decomposition analysis on **5**,[49] partitioned as composed by the fragments $[Ru_2IrCl_4(CO)_7]^-$ and $[IrCl_2(CO)_2]^-$. No negative charge donation from $[Ru_2IrCl_4(CO)_7]^-$ to $[IrCl_2(CO)_2]^-$ was calculated, while 0.17 electrons are transferred in the reverse process.

## Catalytic tests

$[NEt_4][\mathbf{2}]$ was tested as the catalyst precursor for transfer hydrogenation of 4-fluoroacetophenone using $^i$PrOH as a solvent and a hydrogen source (Table 2). Conversion was determined by $^{19}$F NMR spectroscopy comparing the integral of the resonance of the substrate 4-fluoroacetophenone with that of its unique hydrogenation product, that is, 4-F-α-methylbenzylalcohol [1-(4-fluorophenyl)ethan-1-ol]. The catalytic tests were performed at $^i$PrOH refluxing temperature (82 °C), using 1, 2.5 or 5 mol% of $[NEt_4][\mathbf{2}]$ per mol of a substrate, both with and without a base (KO$^t$Bu). All catalytic tests were carried out at least three times using different cluster catalyst precursor batches (including crystalline batches), resulting in highly reproducible results. This seems to exclude the involvement of impurities in the catalytic process. Mass balance has been checked using α,α,α-trifluorotoluene as the internal standard for $^{19}$F NMR analysis.

Control experiments include reactions without any catalyst (with and without a base), as well as reactions with $RuCl_3$, $IrCl_3$, $[PPN][Ir(CO)_4]$ and $[Ir(COD)Cl]_2$ as potential catalyst precursors. All these control tests resulted in almost zero conversion after 5 and 24 h, ruling out the presence of any background reaction under the experimental conditions adopted for the catalytic tests (Table S1 in the ESI†). The homometallic cluster $[NEt_4][\mathbf{1}]$ was previously tested as the catalyst precursor under similar experimental conditions, and the results are summarized in Table 2 for the sake of comparison.[50]

Conversions recorded after 5 h (0–58%) and 24 h (42–92%) indicate some catalytic activity under all the experimental conditions considered, but a long induction period (Table 2). Moreover, spectroscopic analyses (IR spectroscopy, $^1$H NMR spectroscopy and ESI-MS) of the reaction mixtures at the end of the catalytic tests showed the presence in solution of mixtures

Table 2 Catalytic transfer hydrogenation of 4-fluoroacetophenone with heterometallic $[NEt_4][\mathbf{2}]$ compared to that with homometallic $[NEt_4][\mathbf{1}]$

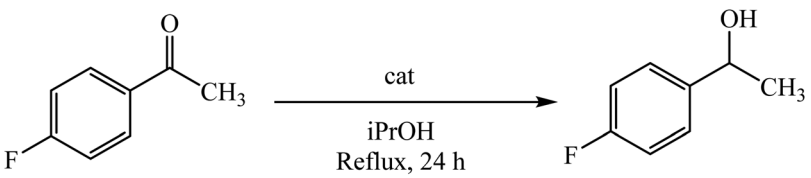


| Entry | Cat | Cat (mol%) | KO$^t$Bu (mol%) | Conversion (%) 1 h | Conversion (%) 3 h | Conversion (%) 5 h | Conversion (%) 24 h |
|---|---|---|---|---|---|---|---|
| 1-2 | | 5 | 10 | 0 | 16 | 20 | 84 |
| 2-2 | | 5 | — | 0 | 0 | 0 | 52 |
| 3-2 | | 2.5 | 10 | 24 | 42 | 58 | 87 |
| 4-2 | $[NEt_4][\mathbf{2}]$ | 1 | 4 | 10 | 24 | 34 | 54 |
| 5-2 | | 1 | 10 | 13 | 34 | 46 | 86 |
| 6-2 | | 1 | — | 0 | 5 | 12 | 42 |
| 7-2 | | 1 | 20 | 0 | 27 | 46 | 92 |
| 1-1 | | 5 | 10 | 0 | 7 | 10 | 50 |
| 2-1 | | 5 | — | 0 | 19 | 37 | 92 |
| 3-1 | $[NEt_4][\mathbf{1}]$ | 2.5 | — | 0 | 17 | 24 | 82 |
| 4-1 | | 1 | 10 | 0 | <5 | 11 | 19 |
| 5-1 | | 1 | — | 0 | 0 | 18 | 80 |

General conditions: catalyst (3, 7.5 or 15 μmol, 1, 2.5 or 5 mol%), $^i$PrOH (5 mL), KO$^t$Bu (4, 10 or 20 mol% when added), and 4-fluoroacetophenone (36.5 μL, 300 μmol), $T$ = 82 °C, $N_2$ atmosphere; the conversions were determined by $^{19}$F NMR spectroscopy. All entries are the average of at least three independent catalytic runs.

 

of carbonyl clusters (Fig. S20–S28 in the ESI†), including hydrides and heterometallic Ru–Ir clusters, ruling out cluster breakdown to mononuclear complexes or nanoparticles as the major event.

Using [$NEt_4$][**2**] as the catalyst precursor, there is a clear beneficial effect after the addition of KO$^t$Bu. Indeed, the conversion at 24 h increases from 42 to 52% (no base) to 54 to 92% (KO$^t$Bu, 4–10–20 mol % respect to the substrate). Heterometallic Ru–M (M = Cu, Ag, Au) carbonyl clusters displayed a similar improvement of the conversion after addition of a base,[50] whereas the opposite trend was observed with the homometallic Ru precursor [$NEt_4$][**1**]. This is somehow indicative of the fact that [$NEt_4$][**2**] and [$NEt_4$][**1**] follow different activation and/or catalytic paths. It is noteworthy that the highest conversion recorded with the heterometallic precursor (92%) was obtained after 24 h employing 1 mol% of [$NEt_4$][**2**] and 20 mol% of KO$^t$Bu. In the case of the homometallic precursor, the same conversion was obtained after 24 h with 5 mol% of [$NEt_4$][**1**] and no base. The results obtained with [$NEt_4$][**2**] are comparable to those previously reported for heterometallic Ru–Cu and Ru–Ag carbonyl clusters, and superior to Ru–Au ones.[50]

It seems that the catalytic process employing [$NEt_4$][**2**] as the catalyst precursor requires a strong base. Indeed, similar results were obtained using NaOMe instead of KO$^t$Bu (Table 3), whereas employing a weaker base such as $NEt_3$ resulted in a conversion comparable to that observed without a base.

Some catalytic tests with [$NEt_4$][**2**] have been repeated adding metallic mercury (Table S3 in the ESI†). This is a well-known method described in the literature in order to remove metal particles and eliminate the heterogeneous contribution to catalysis. It resulted that mercury had a limited effect on catalytic tests in the presence of [$NEt_4$][**2**], suggesting that catalysis is mainly homogeneous. When the base KO$^t$Bu is not used, the results are comparable to those without mercury, if not better, while in the presence of 10 mol% of base, the conversion of the substrate is below expectations. This anomaly in the yield could be expected due to the presence of the metallic Hg itself, more than to the heterogeneous inhibition's role of the mercury, because the latter should cause no activities at all.

Further catalytic tests were performed using **3** and [$NEt_4$]$_2$[**4**] instead of [$NEt_4$][**2**] as the catalyst precursors (Table 4). In the absence of any base, both **3** and [$NEt_4$]$_2$[**4**] displayed very poor conversions (13–15%) compared to [$NEt_4$][**2**] (42%). Conversely, in the presence of KO$^t$Bu (10 mol % per mol of substrate), high conversions were observed for all the three catalyst precursors. Nonetheless, in the case of [$NEt_4$]$_2$[**4**], several unknown resonances were present in the $^{19}$F NMR spectra after catalysis. These are likely to be due to condensation products, in addition to the main hydrogenation reaction. It is noteworthy that such selectivity problems have been observed only by using [$NEt_4$]$_2$[**4**] as the catalyst precursor, whereas complete selectivity to 4-F-α-methylbenzylalcohol was usually observed for all other Ru-based carbonyl clusters employed, both heterometallic and homometallic.

Combined IR spectroscopy, $^1$H NMR spectroscopy and ESI-MS analyses were performed after heating the catalyst precursors in $^i$PrOH at refluxing temperature, with and without bases, as well as with and without substrates in stoichiometric amounts, in order to gain some insights into the carbonyl species present in solution at the end of catalysis (Fig. S20–S28 in the ESI†). These experiments showed the presence of mixtures of products, including heterometallic carbonyl clusters and carbonyl hydrides. During all these experiments, there was no evidence of any stoichiometric product between the catalyst precursors and the substrate, or of the formation of unsaturated species. Thus, it was not possible to devise any plausible reaction pathway for the catalytic process.

Further reactivity tests conducted in a $^i$PrOH solution showed, thanks to IR spectroscopy and $^1$H NMR spectroscopy, that all the three $[H_{3-n}Ru_3Ir(CO)_{12}]^{n-}$ ($n$ = 0–2) species are quickly deprotonated at room temperature to give quantitatively cluster **4** when 10 mol % of KO$^t$Bu is added. Further experiments carried out under the same conditions but with 24 hours of reflux also showed the formation of $[H_3Ru_4(CO)_{12}]^-$ (see below). It must be remarked that $[H_3Ru_4(CO)_{12}]^-$ displays poorer catalytic activity than **2**, **3** and **4** in the presence of a base (Table 5), further supporting the involvement of heterometallic species during catalysis. However, in the presence of the substrate, the composition of the reaction mixture after 24 h diverges for the three compounds **4**, **2** and **3**, evidencing a completely different reaction path, according to the results obtained (Table 4).

When [$NEt_4$][**2**] was employed, it was possible to identify the same species among the carbonyl hydrides species present at the end of the catalytic process. Some homometallic species such as **1** and $[H_3Ru_4(CO)_{12}]^-$ were[51] identified in some experiments, as mentioned above; however, the main compound at the end of the catalytic experiments is [$NEt_4$][**2**] (Fig. S24 in the ESI†), and no mononuclear fragments were detected from the ESI-MS analysis. Overall, it seems that the catalyst precursor **2**

Table 3 Catalytic transfer hydrogenation of 4-fluoroacetophenone with heterometallic [$NEt_4$][**2**] with different bases

| Entry | Cat | Cat (mol%) | Base (10 mol%) | Conversion (%) 1 h | Conversion (%) 3 h | Conversion (%) 5 h | Conversion (%) 24 h |
|---|---|---|---|---|---|---|---|
| 1-2 | | 1 | NaOMe | 35 | 49 | 61 | 88 |
| 2-2 | [$NEt_4$][2] | 1 | $NEt_3$ | 0 | 0 | 0 | 42 |
| 3-2 | | 1 | KO$^t$Bu | 13 | 34 | 46 | 86 |

General conditions: catalyst (3 μmol, 1% mol/mol), $^i$PrOH (5 mL), KO$^t$Bu or $NEt_3$ or NaOMe (10 mol %), and 4-fluoroacetophenone (36.5 μL, 300 μmol), $T$ = 82 °C, and $N_2$ atmosphere; the conversions were determined by $^{19}$F NMR spectroscopy. All entries are the average of at least three independent catalytic runs.

Table 4 Catalytic transfer hydrogenation of 4-fluoroacetophenone with heterometallic $[NEt_4]$[**2**], **3** and $[NEt_4]_2$[**4**]

| Entry | Cat | Cat (mol %) | KO$^t$Bu (mol %) | Conversion (%) 1 h | Conversion (%) 3 h | Conversion (%) 5 h | Conversion (%) 24 h |
|---|---|---|---|---|---|---|---|
| 1-2 | $[NEt_4]$[**2**] | 1 | 10 | 13 | 34 | 46 | 86 |
| 2-2 | | 1 | / | 0 | 5 | 12 | 42 |
| 1-3 | **3** | 1 | 10 | 0 | 16 | 24 | 81 |
| 2-3 | | 1 | / | 0 | 0 | 0 | 13 |
| 1-4 | $[NEt_4]_2$[**4**] | 1 | 10 | 29 | 45 | 52 | 100(80)[a] |
| 2-4 | | 1 | / | 0 | 4 | 6 | 15 |

General conditions: catalyst (3 μmol, 1% mol/mol), $^i$PrOH (5 mL), KO$^t$Bu (10 mol % when needed), and 4-fluoroacetophenone (36.5 μL, 300 μmol), $T$ = 82 °C, and $N_2$ atmosphere; the conversions were determined by $^{19}$F NMR spectroscopy. All entries are the average of at least three independent catalytic runs. [a] The selectivity of the product is 80%; there is evidence of other fluorinated compounds, in contrast with all the other experiments.

Table 5 Catalytic transfer hydrogenation of 4-fluoroacetophenone with homometallic $[NEt_4][H_3Ru_4(CO)_{12}]$

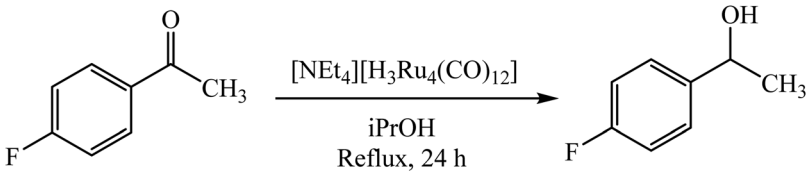


| Entry | Cat | Cat (mol %) | KO$^t$Bu (mol %) | Conversion (%) 1 h | Conversion (%) 3 h | Conversion (%) 5 h | Conversion (%) 24 h |
|---|---|---|---|---|---|---|---|
| 1 | $[NEt_4][H_3Ru_4(CO)_{12}]$ | 1 | / | 0 | 0 | 10 | 44 |
| 2 | | 1 | 10 | 13 | 44 | 45 | 48 |

General conditions: catalyst (3 μmol, 1 mol %), $^i$PrOH (5 mL), KO$^t$Bu (10 mol % when needed), and 4-fluoroacetophenone (36.5 μL, 300 μmol), $T$ = 82 °C, and $N_2$ atmosphere; the conversions were determined by $^{19}$F NMR spectroscopy. All entries are the average of at least three independent catalytic runs.

is in part transformed and in part recovered intact at the end of the process. All the not yet identified species, found at the end of the reactivity experiments, have a molecular mass compatible with at least a bi or trimetallic metal core cluster. In

Table 6 Hydrogenation of *trans*-cinnamaldehyde with heterometallic $[NEt_4]$[**2**]

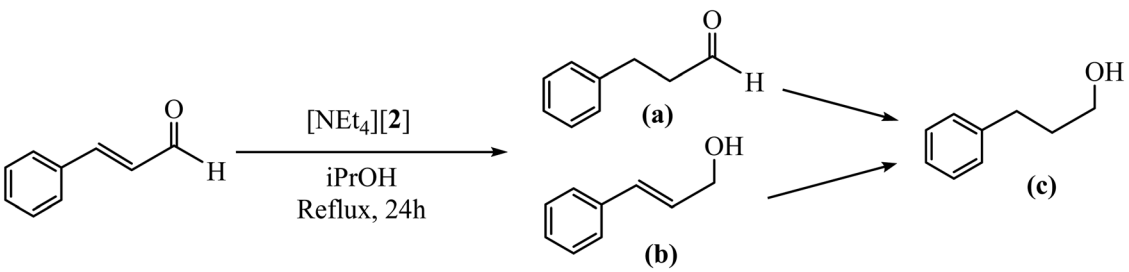


| Entry | Time (h) | Pressure (bar) | Substrate conversion (%) | Yield (**a**) (%) | Yield (**b**) (%) | Yield (**c**) (%) |
|---|---|---|---|---|---|---|
| 1-2 | 24 | 60 $H_2$ | >99 | 0 | 0 | >99 |
| 2-2 | 24 | 30 $H_2$ | >99 | 6 | 0 | 94 |
| 3-2 | 24 | 10 $H_2$ | >99 | 4 | 20 | 76 |
| 4-2 | 3 | 60 $H_2$ | >99 | 17 | 8 | 75 |
| 5-2 | 3 | 30 $H_2$ | >99 | 23 | <5 | 77 |
| 6-2 | 3 | 10 $H_2$ | 81 | 27 | 10 | 44 |
| 7-2 | 24 | 1 $H_2$ | 85 | 26 | 24 | 35 |
| 8-2 | 3 | 1$H_2$ | 49 | <5 | <5 | 49 |
| 9-2 | 24 | 1 $N_2$ | 43 | 0 | 40 | 3 |
| 10-2 | 3 | 1 $N_2$ | 54 | 0 | 54 | 0 |

General conditions entries 1–6: catalyst (18 μmol, 1 mol%), $^i$PrOH (30 mL) and *trans*-cinnamaldehyde (228 μL, 1800 μmol), $T$ = 82 °C, and $H_2$ atmosphere; the conversions were determined by $^1$H NMR spectroscopy. All entries are the average of at least three independent catalytic runs. Catalytic tests were performed using the autoclave Parr reactor.General conditions entries 7–10: catalyst (3 μmol, 1 mol%), $^i$PrOH (5 mL) and *trans*-cinnamaldehyde (38 μL, 300 μmol), $T$ = 82 °C, and $N_2$ or $H_2$ atmosphere; the conversions were determined by $^1$H NMR spectroscopy. All entries are the average of at least three independent catalytic runs.

 

Table 7 Hydrogenation of *trans*-cinnamaldehyde with heterometallic [$NEt_4$][**2**] using toluene as the solvent

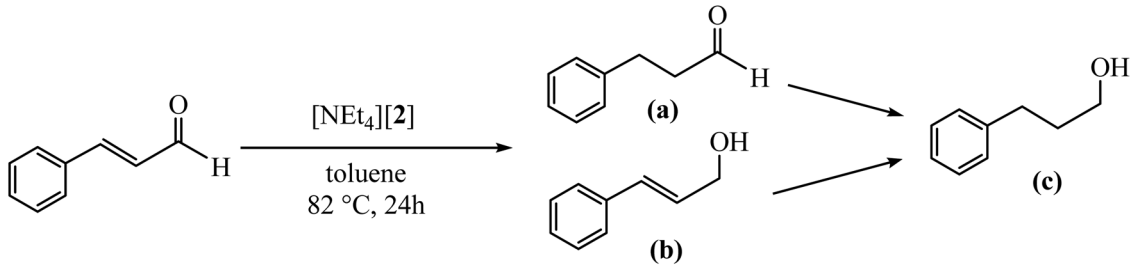


| Entry | Time (h) | Pressure (bar) | Substrate conversion (%) | Yield (**a**) (%) | Yield (**b**) (%) | Yield (**c**) (%) |
|---|---|---|---|---|---|---|
| 1-2 | 24 | 1 $H_2$ | 31 | 21 | <5 | 10 |
| 2-2 | 3 | 1 $H_2$ | 19 | 10.5 | <5 | <5 |
| 3-2 | 3 | 30 $H_2$ | 92 | 16 | 13 | 63 |
| 4-2 | 24 | 30 $H_2$ | >95 | 8 | <5 | 87 |

General conditions entries 1 and 2: catalyst (3 μmol, 1 mol%), toluene (5 mL) and *trans*-cinnamaldehyde (38 μL, 300 μmol), $T$ = 82 °C, and $H_2$ atmosphere; the conversions were determined by $^1$H NMR spectroscopy. All entries are the average of at least three independent catalytic runs.General conditions entries 3 and 4: catalyst (18 μmol, 1 mol%), toluene (30 mL) and *trans*-cinnamaldehyde (228 μL, 1800 μmol), $T$ = 82 °C, and $H_2$ atmosphere; the conversions were determined by $^1$H NMR spectroscopy. All entries are the average of at least three independent catalytic runs. Catalytic tests were performed using the autoclave Parr reactor.

addition, control experiments (Table S1 in the ESI†), using ruthenium and iridium salts, have been conducted to prove the little or no influence of oxidised metal ions in the catalytic activity, since their formation can arise from the decomposition of the clusters structures. In all cases, these results seem to indicate that cluster breakdown to monometallic species or metal nanoparticles is not the major event in solution during catalysis.

Heterometallic cluster [$NEt_4$] [**2**] was also tested in the hydrogenation of *trans*-cinnamaldehyde in $^i$PrOH at refluxing temperature under both a $N_2$ atmosphere and a $H_2$ atmosphere. Catalytic tests were performed without a base in order to avoid side reactions, such as aldol condensation. Under these conditions, three different hydrogenation products can be obtained (Table 6), depending on the hydrogenation site: the saturated aldehyde (**a**), if hydrogenation occurs on the C=C bond; the unsaturated alcohol (**b**), if the C=O bond is hydrogenated; the saturated alcohol (**c**), which is formed when both C=C and C=O are hydrogenated. Conversions and yields were determined by $^1$H NMR spectroscopy at the end of the catalytic tests.

Performing the reaction under a $N_2$ atmosphere, the conversion is moderate but the selectivity is very high towards (**b**). This is consistent with the fact that, under these conditions, hydrogenation occurs *via* hydrogen transfer from $^i$PrOH, which is more selective for the polar C=O bond. The low conversion observed is probably due to the fact that no base has been added. Indeed, as shown by using 4-F-acetophenone as the substrate, the catalytic performances of [$NEt_4$][**2**] for H-transfer to C=O bonds seem to be enhanced by strong bases.

The conversion is considerably increased under $H_2$ at atmospheric pressure, but the selectivity is low, since a mixture of (**a**), (**b**) and (**c**) is obtained. This is due to the fact that, under these experimental conditions, both H-transfer from $^i$PrOH and hydrogenation from $H_2$ occur, the former targeting preferentially the polar C=O bond and the latter the C=C bond. Indeed, by performing the catalytic test under $H_2$ (1 bar) in toluene (entries 1 and 2 in Table 7), the conversion is again low, but the major product is (**a**).

Further catalytic tests were performed in $^i$PrOH at a $H_2$ pressure (10–60 bar) for 24 h (Table 6). At a high $H_2$ pressure (30–60 bar), the conversion is almost quantitative, and selectivity towards the fully hydrogenated product (**c**) is observed, for both long short reaction times (3 and 24 h). Lowering the $H_2$ pressure to 10 bar results in a decreased conversion just a 3 h of reaction, and a mixture of the three hydrogenation and H-transfer products.

Performing the catalytic test for 3 h at 60 bar $H_2$ results in 80% conversion and (**a**) is the major product (46% yield) followed by (**c**) (25%) and traces of (**b**) (9%). These results suggest that hydrogenation mainly occurs *via* $H_2$ at a high pressure, whereas H-transfer becomes more significant at lower $H_2$ pressures.

This point was further supported by performing the reactions in toluene rather than $^i$PrOH (Table 7). Significant amounts of (**a**) are formed, especially operating at a low $H_2$ pressure and/or with a short reaction time. Increasing the $H_2$ pressure and reaction time, (**c**) becomes the major products, whereas the formation of (**b**) is always limited.

## Conclusions

Three heterometallic Ru–Ir hydride carbonyl clusters **2**–**4** were prepared and fully characterized using spectroscopic methods, as well as SC-XRD in the case of **2** and **3**. The location of the hydride ligands was further corroborated by DFT studies. Even though **2**–**4** may be reversibly inter-converted by protonation/deprotonation reactions, they show a different stereochemistry of the ligands, in view of the different charges and number of hydrides. This indicates a rapid ligand rearrangement upon addition/removal of H-atoms. At the same time, it seems that the stereochemistry of CO and hydride ligands around these tetrahedral clusters is the result of a subtle balance between the overall

charge of the cluster (and thus π-back-donation from the metal core to the carbonyls), and steric effects (that is, the number of CO and H ligands). This is further corroborated by comparison with related $[H_{3-n}Ru_3M(CO)_{12}]^{n-}$ and $[H_{3-n}Fe_3M(CO)_{12}]^{n-}$ ($n$ = 0–2; M = Co, Rh, Ir). The ability of ligands to rapidly rearrange around the metal core of molecular clusters and nanoclusters is enables them for their potential application in homogeneous catalysis.

Clusters **2**–**4** display some activities as catalyst precursors in the transfer hydrogenation of 4-fluoroacetophenone. The fact that catalyst loading and addition of a base have a different effect on **2**–**4** as compared to that on the homometallic cluster **1** suggests that their heterometallic nature somehow aids the catalytic process, as also found previously for Ru–M (M = Cu, Ag, Au) clusters.[50] Cluster **2** is also active as the catalyst precursor in the hydrogenation of *trans*-cinnamaldehyde. Depending on the solvent, atmosphere ($N_2$ or $H_2$) and $H_2$ pressure, both a hydrogen transfer mechanism and direct hydrogenation by $H_2$ are observed.

As a final remark, the present findings seem to confirm the synergistic effects of Ru–Ir systems evidenced in the Introduction section. These might be, at least in part, due to the capacity of Ir to form stronger bonds than Ru and/or to some slight polarization of the heterometallic Ru–Ir bonds.

# Experimental

### General procedures

All reactions and sample manipulations were carried out using standard Schlenk techniques under nitrogen and in dried solvents. All the reagents were commercial products (Aldrich) of the highest purity available and used as received, except $[NEt_4][HRu_3(CO)_{11}]$,[41] $[PPN][HRu_3(CO)_{11}]$,[52] $K[Ir(CO)_4]$, $[PPN][Ir(CO)_4]$, $[NEt_4][Rh(CO)_4]$,[53] and $[Ir(COD)Cl]_2$,[54] which have been prepared according to the literature. Analyses of C, H and N were performed using a Thermo Quest Flash EA 1112NC instrument. IR spectra were recorded using a PerkinElmer Spectrum One interferometer in $CaF_2$ cells. $^1H$ and $^{19}F$ NMR measurements were performed using a Varian Mercury Plus 400 MHz instrument. The proton chemical shifts were referenced to the non-deuterated aliquot of the solvent. The fluorine chemical shifts were referenced to external $CCl_3F$. ESI mass spectra were recorded using a Waters Micromass ZQ4000 instrument using $CH_3OH$ as the solvent (source temperature = 150 °C; capillary voltage = 2.54 kV; infusion flow = 20 μL $min^{-1}$; cone voltage = 10 V). Structure drawings have been performed with SCHAKAL99.[55]

### Synthesis of $[NEt_4][H_2Ru_3Ir(CO)_{12}]$ ($[NEt_4][2]$) from $[Ir(COD)Cl]_2$

$$[NEt_4][HRu_3(CO)_{11}] + [Ir(COD)Cl]_2 \xrightarrow[RT,30\,min]{CH_2Cl_2,H_2} [NEt_4][H_2Ru_3Ir(CO)_{12}]$$

$[Ir(COD)Cl]_2$ (0.181 g, 0.270 mmol) was added as a solid to a solution of $[NEt_4][\mathbf{1}]$ (0.400 g, 0.539 mmol) in $CH_2Cl_2$ (20 mL) under a hydrogen atmosphere. The resulting mixture was stirred at room temperature for 30 min. Then, the solvent was removed under reduced pressure, and the residue was washed with water (40 mL) and toluene (20 mL) and then extracted with $CH_2Cl_2$ (15 mL). The brown $CH_2Cl_2$ solution was layered with n-pentane (30 mL), affording crystals of $[NEt_4][\mathbf{2}]$ suitable for SC-XRD (yield 0.390 g, 75% based on Ru).

$[NEt_4]_4[\mathbf{2}]\cdot CH_3CN$: $C_{20}H_{22}IrNO_{12}Ru_3$ (963.79): calcd (%): C 24.92, H 2.30, N 1.45; found: C 25.09, H 2.17, N 1.58. IR ($CH_2Cl_2$, 298 K) $\nu_{CO}$: 2078(w), 2041(m), 2005(vs), 1973(m), 1797(w) $cm^{-1}$. IR (Nujol, 298 K) $\nu_{CO}$: 2077(w), 2034(s), 2001(vs), 1935(m), 1792(w) $cm^{-1}$. $^1H$ NMR (400 MHz, $CD_2Cl_2$, 298 K) $\delta$: −20.7 ppm. ESI-MS ($m/z$): ES- 835 $[M]^-$; ES+ 130 $[NEt_4]^+$.

### Synthesis of $H_3Ru_3Ir(CO)_{12}$ (3)

$$[NEt_4][H_2Ru_3Ir(CO)_{12}] \xrightarrow[RT,30\,min]{1.5\,eq.HBF_4} H_3Ru_3Ir(CO)_{12}$$

A solution of $HBF_4\cdot Et_2O$ (42.3 μL, 0.311 mmol) was added dropwise to a solution of $[NEt_4][\mathbf{2}]$ (0.200 g, 0.207 mmol) in $CH_2Cl_2$ (20 mL) under a nitrogen atmosphere. The resulting mixture was stirred at room temperature for 30 min. Then, the solvent was removed under reduced pressure, and the residue was washed with water (20 mL), and extracted with THF (10 mL). The orange-red THF solution was layered with *n*-hexane (30 mL) and stored at −20 °C, affording crystals of **3** suitable for SC-XRD (yield 0.130 g, 75% based on Ru).

**3**: $C_{12}H_3IrO_{12}Ru_3$ (834.55): calcd (%): C 17.27, H 0.36; found: C 17.42, H 0.59. IR (THF, 298K) $\nu_{CO}$: 2078(vs), 2064(m), 2049(s), 2029(m), 2018(m) $cm^{-1}$. IR (Nujol, 298 K) $\nu_{CO}$: 2075(m), 2048(s), 2023(vs), 2003(vs) $cm^{-1}$. $^1H$ NMR (400 MHz, $CD_2Cl_2$, 298 K) $\delta$(ppm): −17.8 ppm. ESI-MS ($m/z$): **3** is deprotonated to **2** during ESI-MS analysis.

### Synthesis of $[PPN]_2[HRu_3Ir(CO)_{12}]$ ($[PPN]_2[\mathbf{4}]$) from $[PPN][Ir(CO)_4]$

$$[PPN][Ir(CO_4)] + [PPN][HRu_3(CO)_{11}] \xrightarrow[Reflux,48\,h]{THF} [PPN]_2[HRu_3Ir(CO)_{12}]$$

$[PPN][Ir(CO_4]$ (0.252 g, 0.299 mmol) was added as a solid to a solution of $[PPN][\mathbf{1}]$ (0.327 g, 0.299 mmol) in THF (20 mL) under a nitrogen atmosphere. The resulting mixture was stirred at reflux temperature for 48 h. Then, the solvent was removed under reduced pressure, and the residue was washed with water (20 mL) and toluene (20 mL) and then extracted with acetone (15 mL). The brown acetone solution was layered with *n*-hexane (30 mL), affording crystals of $[PPN]_2[\mathbf{4}]$ (yield 0.457 g, 80% based on Ru). Unfortunately, the quality of the crystals was low hampering a detailed structural analysis. Unit cell parameters are herein included as a preliminary analytical information: crystal system, trigonal; space group, $P\bar{3}$; $a$ = 24.2175(14) Å, $b$ = 24.2175(14) Å, $c$ = 12.3732(8) Å, $\alpha$ = 90°, $\beta$ = 90°, $\gamma$ = 120°.

$[PPN]_2[\mathbf{4}]$: $C_{84}H_{61}IrN_2O_{12}P_4Ru_3$ (1909.63): calcd (%): C 52.83, H 3.22, N 1.47; found: C 52.64, H 2.87, N 1.78. IR ($CH_2Cl_2$, 298 K) $\nu_{CO}$: 2023(w), 1976(s), 1961(vs), 1917(m), 1767(m), 1751(m) $cm^{-1}$. IR (Nujol, 298 K) $\nu_{CO}$: 2025(w), 2020(w), 1971(s), 1950(vs), 1915(s), 1760(m), 1755(m) $cm^{-1}$. $^1H$ NMR (400 MHz, acetone $d_6$, 298 K) $\delta$: −19.9 ppm. ESI-MS ($m/z$): **4** is protonated to **2** during ESI-MS analysis.

 

**Synthesis of $[NEt_4]_2[HRu_3Ir(CO)_{12}]$ ($[NEt_4]_2$[4]) from $[NEt_4]$[2]**

$$[NEt_4][H_2Ru_3Ir(CO)_{12}] \xrightarrow[RT,30\,min]{3\,eq.KO^tBu,\ CH_3CN} [NEt_4]_2[HRu_3Ir(CO)_{12}]$$

$KO^tBu$ (0.0700 g, 0.624 mmol) was added in three aliquots as a solid to a solution of $[NEt_4]$[**2**] (0.200 g, 0.208 mmol) in $CH_3CN$ (15 mL). The resulting mixture was stirred at room temperature for 30 min. Then, the solvent was removed under reduced pressure and the residue was washed with water (20 mL) and toluene (10 mL) and then extracted with $CH_3CN$ (10 mL). The presence of **4** in solution has been further corroborated by IR and $^1$H NMR spectroscopy analyses, compared with those obtained with the crystals of $[PPN]_2$[**4**] (yield 0.215 g, 95% based on Ru).

$[NEt_4]_2$[**4**]: $C_{28}H_{41}IrN_2O_{12}Ru_3$ (1093.06): calcd (%): C 30.77, H 3.78, N 2.56; found: C 30.52, H 3.94, N 2.34. IR ($CH_3CN$, 298 K) $\nu_{CO}$: 1979(s), 1959(vs), 1910(m), 1759(m) $cm^{-1}$. $^1$H NMR (400 MHz, $CD_2Cl_2$, 298 K) $\delta$(ppm): −19.4 ppm.

**Synthesis of $[NEt_4]_2[HRu_3Ir(CO)_{12}]$ ($[NEt_4]_2$[4]) from $K[Ir(CO)_4]$**

$$K[Ir(CO_4)]+[NEt_4][HRu_3(CO)_{11}] \xrightarrow[60\,^\circ C,18\,h]{DMSO} [HRu_3Ir(CO)_{12}]^{2-} \xrightarrow{[NEt_4]Br/H_2O} [TEA]_2[HRu_3Ir(CO)_{12}]$$

$[NEt_4]$[**1**] (0.300 g, 0.404 mmol) was added as a solid to a DMSO (5 mL) solution of $K[Ir(CO_4)]$ (0.139 g, 0.404 mmol) under a nitrogen atmosphere. The resulting mixture was stirred at 60 °C for 18 h. Then, product **4** was precipitated through the dropwise addition of the DMSO solution to a saturated $H_2O$ solution of $[NEt_4]Br$. The solid was filtered and washed with water (20 mL), toluene (10 mL) and extracted with acetone (15 mL). The presence of **4** in solution has been further corroborated by IR and $^1$H NMR spectroscopy analyses, compared with those obtained with the crystals of $[PPN]_2$[**4**] (yield 0.287 g, 65% based on Ru).

$[NEt_4]_2$[**4**]: $C_{28}H_{41}IrN_2O_{12}Ru_3$ (1093.06): calcd (%): C 30.77, H 3.78, N 2.56; found: C 30.91, H 3.62, N 2.29. IR ($CH_2Cl_2$, 298 K) $\nu_{CO}$: 2023(w), 1976(s), 1961(vs), 1917(m), 1767(m), 1751(m) $cm^{-1}$. $^1$H NMR (400 MHz, acetone $d_6$, 298 K) $\delta$: −19.9 ppm.

**Deprotonation of $H_3Ru_3Ir(CO)_{12}$ (3) to $[NEt_4]_2[HRu_3Ir(CO)_{12}]$ ($[NEt_4]_2$[4]) in DMSO**

A DMSO solution of **3** (0.200 g, 0.240 mmol) was stirred at room temperature for 18 h; IR spectroscopy showed compound **2** as an intermediate and, then, compound **4** in solution at the end of the reaction. Product **4** was precipitated through the dropwise addition of a saturated $H_2O$ solution of $[NEt_4]Br$ to the DMSO solution. The precipitate was filtered and washed with water (20 mL), toluene (10 mL) and extracted with acetone (15 mL). The presence of the compound $[NEt_4]_2$[**4**] in solution has been further corroborated by IR and $^1$H NMR spectroscopy analysis, compared with those obtained with the crystals of $[PPN]_2$[**4**] (yield 0.118 g, 45% based on Ru).

$[NEt_4]_2$[**4**]: $C_{28}H_{41}IrN_2O_{12}Ru_3$ (1093.06): calcd (%): C 30.77, H 3.78, N 2.56; found: C 30.91, H 3.62, N 2.29. IR ($CH_2Cl_2$, 298 K) $\nu_{CO}$: 2023(w), 1976(s), 1961(vs), 1917(m), 1767(m), 1751(m) $cm^{-1}$. $^1$H NMR (400 MHz, acetone $d_6$, 298 K) $\delta$: −19.9 ppm.

**Synthesis of $[NEt_4]_2[HRu_3Rh(CO)_{12}]$ ($[NEt_4]_2$[6])**

$$[NEt_4][Rh(CO)_4] + [NEt_4][HRu_3(CO)_{11}] \xrightarrow[reflux,18\,h]{acetone} [NEt_4]_2[HRu_3Rh(CO)_{12}]$$

$[NEt_4]$[**1**] (0.300 g, 0.404 mmol) was added as a solid to an acetone (15 mL) solution of $[NEt_4][Rh(CO_4)]$ (0.139 g, 0.404 mmol) under a nitrogen atmosphere. The resulting mixture was stirred at 56 °C for 18 h. Then, the solvent was removed under reduced pressure and the residue was washed with water (60 mL), toluene (10 mL), MeOH (20 mL) and extracted with acetone (10 mL). The brown acetone solution was layered with *n*-hexane (40 mL), affording crystals of $[NEt_4]_2$[**6**] suitable for SC-XRD (yield 0.243 g, 60% based on Ru).

$[NEt_4]_2$[**6**]: $C_{28}H_{41}N_2O_{12}RhRu_3$ (1003.75): calcd (%): C 33.50, H 4.12, N 2.79; found: C 33.21, H 4.35, N 2.50. IR (acetone, 298 K) $\nu_{CO}$: 2014(w), 1956(vs), 1936(m), 1903(w). IR (Nujol, 298 K) $\nu_{CO}$: 2015(w), 1957(vs), 1923(s), 1903(s), 1808(w), 1783(m), 1769(m), 1727(m) $cm^{-1}$. $^1$H NMR (400 MHz, acetone $d_6$, 298 K) $\delta$: −15.7 ppm (d, $^1J_{H\text{-}Rh}$ = 17 Hz).

**Synthesis of $[NEt_4]_2[Ru_2Ir_2Cl_6(CO)_9]$ ($[NEt_4]_2$[5])**

$$[NEt_4]_2[H_2Ru_3Ir(CO)_{12}] \xrightarrow[RT,30\,min]{10\,eq.HClEt_2O,\ THF} [NEt_4]_2[Ru_2Ir_2Cl_6(CO)_9]$$

A solution of $HCl{\cdot}Et_2O$ (55.85 μL, 2.07 mmol) was added dropwise to a solution of $[NEt_4]$[**2**] (0.200 g, 0.207 mmol) in THF (15 mL) under a nitrogen atmosphere. The resulting mixture was stirred at room temperature for 30 min. Then, the solvent was removed under reduced pressure, and the residue was washed with water (20 mL) and extracted with THF (10 mL). The orange-red THF solution was layered with *n*-hexane (30 mL) and stored at −20 °C, affording crystals of compound $[NEt_4]_2$[**5**] suitable for SC-XRD (yield 0.136 g, 50% based on Ru).

$[NEt_4]_2$[**5**]: $C_{25}H_{40}Cl_6Ir_2N_2O_9Ru_2$ (1311.83): calcd (%): C 22.89, H 3.07, N 2.14; found: C 23.05, H 2.89, N 2.38. IR (THF, 298K) $\nu_{CO}$: 2048(vs), 2038(m), 2024(s), 2010(s), 1965(s) $cm^{-1}$.

## Substrate 4-fluoroacetophenone

**General procedure for transfer hydrogenation catalytic reactions**

In a 10 mL two-neck round-bottom flask equipped with a condenser, clusters (3 μmol, 1% mol $mol^{-1}$) and $KO^tBu$ (10 or 20% mol $mol^{-1}$ when needed) were dissolved in $^i$PrOH (5 mL) and stirred at reflux temperature under a nitrogen atmosphere for 5 min. Then, 4-fluoroacetophenone (36.5 μL, 300 μmol) was added, and samples were taken at regular intervals (1, 3, 5, and 24 h of reaction). Aliquots (100 μL) were diluted with $CDCl_3$ (0.5 mL), and conversions were determined by $^{19}$F NMR spectroscopy (Fig. S29–S33 in the ESI†).

### Catalytic tests in the presence of an internal standard (mass balance check)

In a 10 mL two-neck round-bottom flask equipped with a condenser, $[NEt_4][\mathbf{2}]$ (3 μmol, 1% mol $mol^{-1}$) and iPrOH (5 mL) were stirred at reflux temperature under a nitrogen atmosphere for 5 min. Then the substrate 4-fluoroacetophenone (36.5 μL, 300 μmol), and α,α,α-trifluorotoluene (36.8 μL, 300 μmol), as the internal standard, were added. Aliquots (100 μL) were diluted with $CDCl_3$ (0.5 mL) and conversions were determined by $^{19}F$ NMR spectroscopy (Fig. S34 in the ESI†).

### Reactivity experiment of $[NEt_4][\mathbf{2}]$, $[NEt_4]_2[\mathbf{4}]$ and 3 in $^{i}$PrOH

In a Schlenk tube equipped with a condenser, clusters and $^{i}$PrOH were stirred at reflux temperature under a nitrogen atmosphere for 5 min, and then 4-fluoroacetophenone (1 mol eq. when needed) and KO$^{t}$Bu (10 mol eq. when needed) were added. After 24 h of reaction, the solvent was removed under reduced pressure, and the crude of the reaction was analyzed by IR spectroscopy, $^1H$ NMR spectroscopy and ESI-MS.

## Substrate *trans*-cinnamaldehyde

### General procedure for reduction catalytic reactions

In a 10 mL two-neck round-bottom flask equipped with a condenser, cluster $[NEt_4][\mathbf{2}]$ (3 μmol, 1% mol $mol^{-1}$) was dissolved in $^{i}$PrOH (5 mL) and stirred at reflux temperature under a nitrogen or hydrogen atmosphere for 5 min. Then *trans*-cinnamaldehyde (38 μL, 300 μmol) was added; the reaction proceeded for 3 or 24 h. After the removal of the solvent under reduced pressure, the crude is extracted with $CDCl_3$ (0.5 mL), and conversions were determined by $^1H$ NMR spectroscopy (Fig. S34–S37 in the ESI†).

### Hydrogenation reactions under high pressure in an autoclave

In a steel autoclave equipped with a controller, a mantel and a thermocouple, cluster $[NEt_4][\mathbf{2}]$ (21 mg, 18 μmol) and *trans*-cinnamaldehyde (228 μL, 1800 μmol) were dissolved in $^{i}$PrOH (30 mL) and stirred at reflux temperature under hydrogen pressure for 3 or 24 h. After the removal of the solvent under reduced pressure, the crude is extracted with $CDCl_3$ (0.5 mL), and conversions were determined by $^1H$ NMR spectroscopy.

### X-ray crystallographic study

Crystal data and collection details for $[NEt_4][\mathbf{2}]$, **3**, $[NEt_4]_2[\mathbf{5}]$, and $[NEt_4]_2[\mathbf{6}]$ are reported in Table S4 in the ESI.† The diffraction experiments were carried out using a Bruker APEX II diffractometer equipped with a PHOTON2 detector using Mo–Kα radiation. Data were corrected for Lorentz polarization and absorption effects (empirical absorption correction SADABS).[56] Structures were solved by direct methods and refined by full-matrix least-squares based on all data using $F^2$.[57] Hydrogen atoms were fixed at calculated positions and refined using a riding model. The presence of hydrides in $[NEt_4][\mathbf{2}]$, **3**, and $[NEt_4]_2[\mathbf{6}]$ has been determined by $^1H$ NMR spectroscopy. Hydride ligands have been placed in the structure based on geometrical considerations, that is, elongation of M–M bonds, stereochemistry of the CO ligands, and steric requirements. Then, their positions have been included in the structural model, and refined isotropically using a riding model. Some restraints have been used for hydrides, as listed below. All non-hydrogen atoms were refined with anisotropic displacement parameters, unless otherwise stated.

As noticed by one referee during revision, there are some problems with these structures. Something has gone seriously wrong with data collection and/or date reduction steps. Nonetheless, there is no question regarding the overall connectivity of the heavy elements. These problems are mainly due to absorption effects. Multi-scan absorption corrections have been applied to all the structures. Indeed, all the crystals are irregular making face indexing very difficult. Despite several attempts, it was not possible to obtain better crystals. Face index corrections instead of multi-scan have sometimes been attempted, without any improvement. Therefore, in some cases, residual electron densities close to heavy atoms are still present after refinement, due to the above mentioned problems in applying absorption corrections to irregular thin plates and needles. In order to help the reader assessing the quality of these structures and related problems, images of residual electron densities, observed and calculated structure factors ($F_{obs}$ *vs.* $F_{calc}$ plot), and fractal dimension plots are included as Fig. S42–S51 in the ESI.†

**[NEt4][2].** The asymmetric unit of the unit cell contains half of a cluster anion (located on *m*) and half of a $[NEt_4]^+$ cation (located on 2). The Et-groups of the $[NEt_4]^+$ cation are disordered and, thus, they have been split into two positions. Similar *U* restraints have been applied to the C and N atoms of the $[NEt_4]^+$ cation (SIMU line in SHELXL, s.u. 0.01). Restraints to bond distances were applied as follows (s.u. 0.02): 1.47 Å for C–N and 1.53 Å for C–C in $[NEt_4]^+$. All Ru–H distances have been restrained to be the same (SADI line in SHELXL, s.u. 0.02).

**3.** The asymmetric unit of the unit cell contains one cluster molecule located on a general position. All Ru–H distances have been restrained to be the same (the SADI line in SHELXL, s.u. 0.02). An anti-bumping restraint (DFIX −3.11 O4 O4_$1 line in SHELXL, s.u. 0.02) was employed in order to remove an unrealistic short inter-molecular O···O contact (2.78 Å).

**[NEt4]2[5].** The asymmetric unit of the unit cell contains one cluster anion and two $[NEt_4]^+$ cations, all located on general positions. One $[NEt_4]^+$ cation is disordered and, therefore, it has been split into two positions during refinement. Similar *U* restraints have been applied to the C and N atoms of the disordered $[NEt_4]^+$ cation (the SIMU line in SHELXL, s.u. 0.01). Restraints to bond distances were applied as follows: (s.u. 0.02): 1.47 Å for C–N and 1.53 Å for C–C in disordered $[NEt_4]^+$. An anti-bumping restraint (DFIX −2.84 O7 O8 line in SHELXL, s.u. 0.02) was employed in order to remove an unrealistic short inter-molecular O···O contact (2.78 Å).

**[NEt4]2[6].** The asymmetric unit of the unit cell contains one cluster anion (located on a general position), one $[NEt_4]^+$ cation (located on a general position), and two halves of two $[NEt_4]^+$ cations (both located on inversion centers). The metal cage of the cluster anion and all the $[NEt_4]^+$ cations are disordered.

 

Therefore, they have been split into two positions and refined using one occupancy factor per each disordered image. In the case of the cluster anion, since the minor image represented less than 10%, only the metal atoms have been included in its model, whereas all atoms (metals and CO ligands) were included in the major image. The crystals are pseudo-merohedrally twinned, with a twin matrix of −1 0 0 0 −1 0 0 0 1. The unique hydride atom was placed on the basis of geometrical and spectroscopic ($^1$H NMR) considerations, and then its position restrained during refinement. Similar *U* restraints have been applied to the C and N atoms of the $[NEt_4]^+$ cations (the SIMU line in SHELXL, s.u. 0.01). Restraints to bond distances were applied as follows (s.u. 0.02): 1.47 Å for C–N and 1.53 Å for C–C in $[NEt_4]^+$; 1.9 for Ru–H and Rh–H in the cluster anion.

## Computational details

Geometry optimizations were performed using the PBEh-3c method, which is a reparametrized version of PBE0[58] (with 42% HF exchange) that uses a split-valence double-zeta basis set (def2-mSVP)[59,60] with ECPs on heavy atoms (28 electrons were included in the core for Ru and Rh and 60 electrons for Ir) and adds three corrections considering dispersion, basis set superposition and other basis set incompleteness effects.[61–63] IR simulations were carried out using the harmonic approximation, from which zero-point vibrational energies and thermal corrections ($T$ = 298.15 K) were obtained.[64] The software used was ORCA version 5.0.3.[65] The output was elaborated using MultiWFN, version 3.8.[66] Cartesian coordinates of the DFT-optimized structures are collected in a separated.xyz file.

## Conflicts of interest

There are no conflicts to declare.

## Acknowledgements

We thank the University of Bologna for financial support.

## References

1 J. Campos, Bimetallic Cooperation across the Periodic Table, *Nat. Rev. Chem.*, 2020, **4**, 696–702.
2 I. G. Powers and C. Uyeda, Metal-Metal Bonds in Catalysis, *ACS Catal.*, 2017, **7**, 936–958.
3 H.-C. Yu and N. P. Mankad, Catalytic Reactions by Heterobimetallic Carbonyl Complexes with Polar Metal-Metal Interactions, *Synthesis*, 2021, 1409–1422.
4 C. Cesari, B. Berti, F. Calcagno, C. Lucarelli, M. Garavelli, R. Mazzoni, I. Rivalta and S. Zacchini, Bimetallic Co-M (M = Cu, Ag, and Au) Carbonyl Complexes Supported by *N*-Heterocyclic Carbene Ligands: Synthesis, Structures, Computational Investigation, and Catalysis for Ammonia Borane Dehydrogenation, *Organometallics*, 2021, **40**, 2724–2735.
5 M. A. Stevens and A. L. Colebatch, Cooperative approaches in catalytic hydrogenation and dehydrogenation, *Chem. Soc. Rev.*, 2022, **51**, 1881–1898.
6 X. Kang, Y. Li, M. Zhu and R. Jin, Atomically precise alloy nanoclusters: syntheses, structures, and properties, *Chem. Soc. Rev.*, 2020, **49**, 6443–6514.
7 X. Zhang, G. Cui, H. Feng, L. Chen, H. Wang, B. Wang, X. Zhang, L. Zheng, S. Hong and M. Wei, Platinum-copper single atom alloy catalysts with high performance towards glycerol hydrogenolysis, *Nat. Commun.*, 2019, **10**, 5812.
8 I. López-Hernández, V. Truttmann, C. Garcia, C. W. Lopes, C. Rameshan, M. Stöger-Pollach, N. Barrabés, G. Rupprechter, F. Rey and A. E. Palomares, AgAu nanoclusters supported on zeolites: Structural dynamics during CO oxidation, *Catal. Today*, 2022, **384–386**, 166–176.
9 T. Zheng, F. Wu, H. Fu, L. Zeng, C. Shang, L. Zhu and Z. Guo, Rational Design of Pt-Pd-Ni Trimetallic Nanocatalysts for Room-Temperature Benzaldehyde and Styrene Hydrogenation, *Chem. – Asian J.*, 2021, **16**, 2298–2306.
10 T. Kawawaki, Y. Imai, D. Suzuki, S. Kato, L. Koboyashi, T. Suzuki, R. Kaneko, S. Hossain and Y. Negishi, Atomically Precise Alloy Nanoclusters, *Chem. – Eur. J.*, 2020, **26**, 16150–16193.
11 Y. Du, H. Sheng, D. Astruc and M. Zhu, Atomically Precise Noble Metal Nanoclusters as Efficient Catalysts: A Bridge between Structure and Properties, *Chem. Rev.*, 2020, **120**, 526–622.
12 C. Cesari, J.-H. Shon, S. Zacchini and L. A. Berben, Metal carbonyl clusters of groups 8-10: synthesis and catalysis, *Chem. Soc. Rev.*, 2021, **50**, 9503–9539.
13 S. Zacchini, Using Metal Carbonyl Clusters To Develop a Molecular Approach towards Metal Nanoparticles, *Eur. J. Inorg. Chem.*, 2011, 4125–4145.
14 Y. Li, M. Zhou and R. Jin, Programmable Metal Nanoclusters with Atomic Precision, *Adv. Mater.*, 2021, **33**, 2006591.
15 M. Zhou, X. Du, H. Wang and R. Jin, The Critical Number of Gold Atoms for a Metallic State Nanocluster: Resolving a Decades-Long Question, *ACS Nano*, 2021, **15**, 13980–13992.
16 *Clusters and Colloids*, ed. G. Schmid, Wiley-VCH, New York, 1994.
17 C. Sun, B. K. Teo, C. Deng, J. Lin, G.-G. Luo, C.-H. Tung and D. Sun, Hydrido-coinage-metal clusters: Rational design, synthetic protocols and structural characteristics, *Coord. Chem. Rev.*, 2021, **427**, 213576.
18 R. Jin and T. Higaki, Open questions on the transition between nanoscale and bulk properties of metals, *Commun. Chem.*, 2021, **4**, 28.
19 C. Femoni, M. C. Iapalucci, F. Kaswalder, G. Longoni and S. Zacchini, The possible role of metal carbonyl clusters in nanoscience and nanotechnologies, *Coord. Chem. Rev.*, 2006, **250**, 1580–1604.
20 I. Ciabatti, C. Femoni, M. C. Iapalucci, G. Longoni and S. Zacchini, Platinum Carbonyl Clusters Chemistry: Four Decades of Challenging Nanoscience, *J. Cluster Sci.*, 2014, **25**, 115–146.
21 C. Cesari, B. Berti, T. Funaioli, C. Femoni, M. C. Iapalucci, D. Pontiroli, G. Magnani, M. Riccò, M. Bortoluzzi,

F. M. Vivaldi and S. Zacchini, Atomically Precise Platinum Carbonyl Nanoclusters: Synthesis, Total Structure, and Electrochemical Investigation of $[Pt_{27}(CO)_{31}]^{4-}$ Displaying a Defective Structure, *Inorg. Chem.*, 2022, **61**, 12534–12544.

22 *Catalysis by Di- and Polynuclear Metal Cluster Complexes*, ed. R. D. Adams and F. A. Cotton, Wiley-VCH, New York, 1998.

23 R. Jin, G. Li, S. Sharma, Y. Li and X. Du, Toward Active-Site Tailoring in Heterogeneous Catalysis by Atomically Precise Metal Nanoclusters with Crystallographic Structures, *Chem. Rev.*, 2021, **121**, 567–648.

24 T. Kawawaki, Y. Kataoka, M. Hirata, Y. Iwamatsu, S. Hossain and Y. Negishi, Toward the creation of high-performance heterogeneous catalysts by controlled ligand desorption from atomically precise metal nanoclusters, *Nanoscale Horiz.*, 2021, **6**, 409–448.

25 P. Buchwalter, J. Rosé and P. Braunstein, Multimetallic Catalysis Based on Heterometallic Complexes and Clusters, *Chem. Rev.*, 2015, **115**, 28–126.

26 S. Haak, A. Neels, H. Stoeckli-Evans, G. Süss-Fink and C. M. Thomas, Fixation and spontaneous dehydrogenation of methanol on a triruthenium-iridium framework: synthesis and structure of the cluster anion $[HRu_3Ir(CO)_{12}(OMe)]^-$, *Chem. Commun.*, 1999, 1959–1960.

27 G. Süss-Fink, S. Haak, V. Ferrand and H. Stoeckli-Evans, The mixed-metal carbonyl cluster anion $[Ru_3Ir(CO)_{13}]^-$: synthesis, molecular structure, fluxionality, reactivity, *J. Chem. Soc., Dalton Trans.*, 1997, 3861–3865.

28 V. Ferrand, G. Süss-Fink, A. Neels and H. Stoeckli-Evans, Triruthenium-iridium clusters containing alkyne ligands: synthesis, structure, and catalytic implications of $[(\mu\text{-H})IrRu_3(CO)_{11}(\mu_3\text{-}\eta^2\text{-PhC}{\equiv}\text{CPh})]$ and $[IrRu_4(CO)_{10}(\mu_4\text{-}\eta^2\text{-PhC}{\equiv}\text{CPh})(\mu\text{-}\eta^2\text{-PhC = CHPh})]$, *J. Chem. Soc., Dalton Trans.*, 1998, 3825–3831.

29 R. D. Adams, P. J. Pellechia, M. D. Smith and Q. Zhang, Iridium-Ruthenium-gold cluster complexes: Structure, and skeletal Rearrangements, *J. Organomet. Chem.*, 2012, **706–707**, 20–25.

30 H. Hamada, Y. Kuwahara, Y. Kintaichi, T. Ito, K. Wakabayashi, H. Iljima and K.-I. Sano, Selective synthesis of $C_2$-oxygenated compounds from synthesis gas over Ir-Ru bimetallic catalysts, *Chem. Lett.*, 1984, 1611–1612.

31 R. E. Fuentes, J. Farell and J. W. Weidner, Multimetallic Electrocatalysts of Pt, Ru, and Ir Supported on Anatase and Rutile $TiO_2$ for Oxygen Evolution in an Acid Environment, *Electrochem. Solid-State Lett.*, 2011, **14**, E5–E7.

32 M. Zlatar, D. Nater, D. Escalera-López, R. M. Joy, P. Pobedinskas, K. Haenen, C. Copéret and S. Cherevko, Evaluating the stability of Ir single atom and Ru atomic cluster oxygen evolution reaction electrocatalysts, *Electrochim. Acta*, 2023, **444**, 141982.

33 J. A. Clayton and R. I. Walton, Development of New Mixed-Metal Ruthenium and Iridium Oxides as Electrocatalysts for Oxygen Evolution: Part I, *Johnson Matthey Technol. Rev.*, 2022, **66**, 393–405.

34 J. Xu, Z. Lian, B. Wei, Y. Li, O. Bondarchik, N. Zhang, Z. Yu, A. Araujo, I. Amorim, Z. Wang, B. Li and L. Liu, Strong Electronic Coupling between Ultrafine Iridium-Ruthenium Nanoclusters and Conductive, Acid-Stable Tellurium Nanoparticle Support for Efficient and Durable Oxygen Evolution in Acidic and Neutral Media, *ACS Catal.*, 2020, **10**, 3571–3579.

35 S. Matsuda, S. Masuda, S. Takano, N. Ichikuni and T. Tsukuda, Synergistic Effect in Ir- or Pt-Doped Ru Nanoparticles: Catalytic Hydrogenation of Carbonyl Compounds under Ambient Temperature and $H_2$ Pressure, *ACS Catal.*, 2021, **11**, 10502–10507.

36 A. J. Saadun, S. Mitchell, H. Bonchev and J. Pérez-Ramírez, Carbon-Supported Bimetallic Ruthenium-Iridium Catalysts for Selective and Stable Hydrodebromination of Dibromomethane, *ChemCatChem*, 2022, **14**, e202101494.

37 M. Chatterjee, A. Chatterjee, M. Kitta and H. Kawanami, Selective controlled transformation of carbon dioxide into a versatile bi-functional multi-carbon oxygenate using a physically mixed ruthenium-iridium catalyst, *Catal. Sci. Technol.*, 2021, **11**, 4719–4731.

38 G. Süss-Fink, S. Haak, V. Ferrand, A. Neels and H. Stoeckli-Evans, Site-selective carbonyl substitution in the mixed-metal cluster anion [H2Ru3Ir(CO)12]–: synthesis and characterization of phosphine, phosphite, arsine and stibine derivatives, *J. Organomet. Chem.*, 1999, **580**, 225–233.

39 H. J. Kakkonen, M. Ahlgrèn, T. A. Pakkanen and J. Pursiainen, Synthesis and structural characterization of [N(PPh3)2][H2Ru3Rh(CO)12], *J. Organomet. Chem.*, 1994, **482**, 279–283.

40 C. Cesari, C. Femoni, M. C. Iapalucci and S. Zacchini, Molecular Fe, Co and Ni carbide carbonyl clusters and nanoclusters, *Inorg. Chim. Acta*, 2023, **544**, 121235.

41 C. Cesari, M. Bortoluzzi, C. Femoni, M. C. Iapalucci and S. Zacchini, Synthesis, molecular structure and fluxional behavior of the elusive $[HRu_4(CO)_{12}]^{3-}$ carbonyl anion, *Dalton Trans.*, 2022, **51**, 2250–2261.

42 C. Cesari, T. Funaioli, B. Berti, C. Femoni, M. C. Iapalucci, F. M. Vivaldi and S. Zacchini, Atomically Precise Ni-Pd Alloy Carbonyl Nanoclusters: Synthesis, Total Structure, Electrochemistry, Spectroelectrochemistry, and Electrochemical Impedance Spectroscopy, *Inorg. Chem.*, 2021, **60**, 16713–16725.

43 C. Cesari, B. Berti, M. Bortoluzzi, C. Femoni, T. Funaioli, F. M. Vivaldi, M. C. Iapalucci and S. Zacchini, From $M_6$ to $M_{12}$, $M_{19}$ and $M_{38}$ molecular alloy Pt-Ni carbonyl nanoclusters: selective growth of atomically precise heterometallic nanoclusters, *Dalton Trans.*, 2023, **52**, 3623–3642.

44 J. Pursiainen and T. A. Pakkanen, Preparation and X-ray crystal structure of $[Ru_3RhH_3(CO)12]$, *J. Chem. Soc., Dalton Trans.*, 1989, 2449–2451.

45 C. Femoni, M. C. Iapalucci, G. Longoni, S. Zacchini and S. Zarra, New Findings in the Chemistry of Iron Carbonyls: The Previously Unreported $[H_{4-n}Fe_4(CO)_{12}]^{n-}$ (n = 1, 2) Series of Clusters, Which Fills the Gap with Ruthenium and Osmium, *Inorg. Chem.*, 2009, **48**, 1599–1605.

46 B. Berti, M. Bortoluzzi, C. Cesari, C. Femoni, M. Hayatifar, M. C. Iapalucci and S. Zacchini, Bimetallic Fe-Ir and Trimetallic Fe-Ir-Au Carbonyl Clusters Containing Hydride and/or Phosphine Ligands: Syntheses, Structures and DFT Studies, *J. Cluster Sci.*, 2021, **32**, 743–753.

 

47 R. Della Pergola, L. Garlaschelli, F. Demartin, M. Manassero, N. Masciocchi and G. Longoni, Synthesis and crystal structure of $[NEt_4]_2[HFe_3Rh(CO)_{12}]$, the first tetranuclear Fe-Rh hydridocarbonyl cluster, *J. Organomet. Chem.*, 1988, **352**, C59–C62.
48 C. Lepetit, P. Fau, K. Fajerwerg, M. L. Kahn and B. Silvi, Topological analysis of the metal-metal bond: A tutorial review, *Coord. Chem. Rev.*, 2017, **345**, 150–181.
49 S. Dapprich and G. Frenking, Investigation of Donor-Acceptor Interactions: A Charge Decomposition Analysis Using Fragment Molecular Orbitals, *J. Phys. Chem.*, 1995, **99**, 9352–9362.
50 C. Cesari, M. Bortoluzzi, F. Forti, L. Gubbels, C. Femoni, M. C. Iapalucci and S. Zacchini, 2-D Molecular Alloy Ru-M (M = Cu, Ag, and Au) Carbonyl Clusters: Synthesis, Molecular Structure, Catalysis, and Computational Studies, *Inorg. Chem.*, 2022, **61**, 14726–14741.
51 C. Cesari, M. Bortoluzzi, C. Femoni, M. C. Iapalucci and S. Zacchini, One-pot atmospheric pressure synthesis of [H3Ru4(CO)12]–, *Dalton Trans.*, 2021, **50**, 9610–9622.
52 A. Béguin, J. M. Soulié and G. Süss-Fink, Bis(triphenylphosphoranylidene)ammonium μ-carbonyl-1κ*C*:2κ*C*-decacarbonyl-1κ$^3$*C*,2κ$^3$,3κ$^4$*C*-μ-hydrido-1κ:2κ-*triangulo*-trirutenate(1–), *Inorg. Synth.*, 1998, **32**, 268–270.
53 L. Garlaschelli, P. Chini and S. Martinengo, New syntheses of the $[Rh(CO)_4]^-$ and $[Ir(CO)_4]^-$ anions, *Gazz. Chim. Ital.*, 1982, **112**, 285–288.
54 J. L. Herde, J. C. Lambert and C. V. Senoff, Cyclooctene and 1.5-cyclooctadiene complexes of iridium(III), *Inorg. Synth.*, 1974, **15**, 18–20.
55 E. Keller, SCHAKAL99; University of Freiburg: Freiburg, *Germany*, 1999.
56 G. M. Sheldrick, SADABS-2008/1-Bruker AXS Area Detector Scaling and Absorption Correction; Bruker AXS: Madison, WI, 2008.
57 G. M. Sheldrick, Crystal Structure Refinement with SCHELXL, *Acta Crystallogr., Sect. C: Struct, Chem*, 2015, **71**, 3–8.
58 S. Grimme, J. G. Brandenburg, C. Bannwarth and A. A. Hansen, Consistent structures and interactions by density functional theory with small atomic orbital basis sets, *J. Chem. Phys.*, 2015, **143**, 054107.
59 F. Weigend and R. Ahlrichs, Balanced basis sets of split valence, triple zeta valence and quadruple zeta valence quality for H to Rn: Design and assessment of accuracy, *Phys. Chem. Chem. Phys.*, 2005, **7**, 3297–3305.
60 F. Weigend, Accurate Coulomb-fitting basis sets for H to Rn, *Phys. Chem. Chem. Phys.*, 2006, **8**, 1057–1065.
61 H. Kruse and S. A. Grimme, geometrical correction for the inter- and intra-molecular basis set superposition error in Hartree-Fock and density functional theory calculations for large systems, *J. Chem. Phys.*, 2012, **136**, 154101.
62 S. Grimme, S. Ehrlich and L. Goerigk, Effect of the damping function in dispersion corrected density functional theory, *J. Comput. Chem.*, 2011, **32**, 1456–1465.
63 S. Grimme, J. Antony, S. Ehrlich and H. A. Krieg, Consistent and accurate ab initio parametrization of density functional dispersion correction (DFT-D) for the 94 elements H-Pu, *J. Chem. Phys.*, 2010, **132**, 154104.
64 C. Cramer, *Essentials of Computational Chemistry*, Wiley, Chichester, 2nd edn, 2004.
65 F. Neese, Software update: The ORCA program system - Version 5.0, *WIREs Comput. Mol. Sci.*, 2022, e1616.
66 T. Lu and F. Chen, Multiwfn: A Multifunctional Wavefunction Analyzer, *J. Comput. Chem.*, 2012, **33**, 580–592.